ACADEMIA
NANO: SCIENCE,
MATERIALS, TECHNOLOGY

Research Article
Published: 2025-06-11
https://doi.org/10.20935/AcadNano7714

Comprehensive benchmarking and user guide for the characterization of CVD-grown transition metal chalcogenides

Bartlomiej Tywoniuk[1,*,†], Michael J. Mohn[2,†], Yanfei Zhao[3,†], Beata M. Szydłowska[1,4], Oliver Hartwig[1], Simona Pace[5,6], Piotr Caban[7], Conor P. Cullen[8], Tibor Lehnert[2], Julian Schulz[2], Prasana K. Sahoo[9], Sachin M. Shinde[9], Alisson R. Cadore[9], Ioannis Paradisanos[9], Osman Balci[9], Andrea C. Ferrari[9], Camilla Coletti[5,6], Niall Mc Evoy[8], Claudia Backes[1,4], Andras Kis[3], Ute Kaiser[2], Mar Garcia Hernandez[10], Georg S. Duesberg[1,*]

Academic Editor: Cesar Moreno

Abstract

Since the discovery of graphene in 2004, there has been rapid progress in research on two-dimensional (2D) material's potential applications with significant impact. Efforts to bring 2D materials closer to industrial production, quality assessment, and standardization still need to be expanded upon. This remains challenging because sophisticated analytics techniques are required to analyze a limited amount of material with high variability due to differences in the synthesis process and the lack of a clear standard for comparing results. Modern methods can evaluate domain size, surface coverage, defects, dopants, mobility, and photoluminescence parameters. Still, it is challenging to understand the structure–property relationship due to external influences such as adsorbates and strain, which can alter results. To address this problem, the Graphene Flagship project conducted an extensive benchmarking study of monolayer molybdenum disulfide grown through chemical vapor deposition by various groups. The study employed a variety of techniques to characterize the material, including optical and transmission electron microscopy, Raman spectroscopy, photoluminescence, X-ray photoelectron spectroscopy, and capacitance-voltage measurements. Herein, we present the results of this comprehensive study and the correlation between various methods.

Keywords: *molybdenum disulfide, MoS2, assessment, CVD*

Citation: Tywoniuk B, Mohn MJ, Zhao Y, Szydłowska BM, Hartwig O, Pace S, et al. Comprehensive benchmarking and user guide for the characterization of CVD-grown transition metal chalcogenides. *Academia Nano: Science, Materials, Technology* 2025;2. https://doi.org/10.20935/AcadNano7714

1. Introduction

Since graphene was discovered in 2004, there has been rapid progress in research on atomically thin two-dimensional materials, with an increasing number of publications discussing new materials on a daily basis. Each of these materials has unique properties and potential applications, e.g., hexagonal boron nitride is used as an insulator, graphene is used as a semi-metal, or molybdenum disulfide is used as a semiconductor. These materials have attracted significant attention because of their distinct properties, which provide insight into low-dimensional physics and offer a unique platform for innovation in various fields, including optics, mechanics, chemistry, and electronics.

The layered transition metal dichalcogenide, molybdenum disulfide (MoS_2), is one of the promising members of the 2D family, with significant potential for practical applications. It is a model system with applications including field-effect transistors [1–4], photodetectors [5, 6], photocatalytic hydrogen production [7], photoelectrochemical cell sensors [8], biomolecule detectors [9], NH_3 sensors [10], solar cells [11–15], photodiodes [16], nano-electromechanical systems (NEMS) resonators [17], and lubricants [18]. Consequently, there is a high demand for reliable and reproducible synthesis methods that can produce monolayered 2D materials.

[1]Institute of Physics and SENS Research Center, University of the Bundeswehr Munich, Werner Heisenberg-Str. 39, 85577 Neubiberg, Germany.
[2]Central Facility for Electron Microscopy, Ulm University, Albert-Einstein-Allee 11, 89081 Ulm, Germany.
[3]Laboratory of Nanoscale Electronics and Structures, Electrical Engineering Institute, Ecole Polytechnique Federale de Lausanne (EPFL), 1015 Lausanne, Switzerland.
[4]Institute of Physical Chemistry, Heidelberg University, The Ruprecht Karl University of Heidelberg, 69117 Heidelberg, Germany.
[5]Center for Nanotechnology Innovation @NEST, Istituto Italiano di Tecnologia, Piazza San Silvestro 12, 56127 Pisa, Italy.
[6]Graphene Laboratories, Istituto Italiano di Tecnologia, Via Morego 30, 16163 Genova, Italy.
[7]Łukasiewicz—Institute of Microelectronics and Photonics, al. Lotników 32/46, 02-668 Warszawa, Poland.
[8]CRANN and AMBER Research Centres and School of Chemistry, Trinity College, University of Dublin, D04 V1W8 Dublin, Ireland.
[9]Cambridge Graphene Centre, University of Cambridge, Cambridge CB30FA, UK.
[10]2D Foundry, Instituto de Ciencia de Materiales de Madrid, Consejo Superior de Investigaciones Cientificas, 28049 Madrid, Spain.
*email: btywoniuk@gmail.com (B.T.); duesberg@unibw.de (G.S.D.)
†These authors contributed equally to this work.

There are two primary methods of creating 2D materials: top–down and bottom–up. The former involves peeling off layers from existing crystals, while the latter involves growing material on a substrate [19, 20]. As the focus of research moves from characterizing TMDs materials to devices, bottom–up techniques are becoming more popular [21]. Next to techniques like molecular beam epitaxy (MBE) or atomic layer deposition (ALD), the most commonly used growth method is chemical vapor deposition (CVD) [22].

Compared to other techniques, CVD is advantageous in terms of its low cost, high throughput, and ability to grow large-area, high-quality monolayers. To obtain large-area, high-quality films, researchers are studying the flux and impact of various precursors, substrates, seeding promoters, and growth parameters, like pressure and temperature [23]. Unfortunately, the complete spectrum of growth conditions and properties is rarely meticulously reported in the literature. Furthermore, often, films or flakes must be transferred to target substrates that are preferable for device fabrication, altering the properties of grown material. Thus, the quality of films varies not only due to growth conditions, which influences domain size, grain boundaries, and stacking order but can also be determined by their substrate and surface contaminants, to name a few parameters.

This report aims to thoroughly investigate MoS_2 fabricated independently at different laboratories across Europe. Samples were grown by chemical vapor deposition at six different institutions. Each research laboratory utilized its setup and parameters for growing monolayered thin-film MoS_2 samples. The authors utilized commonly used and effective analytical techniques to establish a standard for evaluating the quality of 2D materials. The most crucial growth parameters are listed in **Table 1** and further details can be found in Methods and Supplementary materials Table S15. The samples were anonymized for objectivity and easy reference. Optical microscopy, Raman spectroscopy, and X-ray photoelectron spectroscopy (XPS) was performed by Universität der Bundeswehr München, Universität Ulm provided the transmission electron microscope (TEM) and capacitance–voltage (C-V) measurements were obtained by École Polytechnique Fédérale de Lausanne to fully assess the quality of the MoS_2 films. Samples were evaluated independently under the same conditions and using the sets of the same tools.

2. Materials and methods

Data analysis. Where not explicitly mentioned otherwise, the Python [24] programming language was used (version > 3.8) with SciPy [25] libraries (version > 1.5.0) to perform statistical analysis and generate relevant figures [26].

X-ray photoelectron spectroscopy. X-ray photoelectron spectroscopy (XPS) measurements were obtained in a ultra-high vacuum (base pressure 2×10^{-10} mbar) using a PHI VersaProbe III (Chigasaki, Kanagawa, Japan) instrument equipped with a micro-focused monochromated Al Kα source (1486.6 eV) and dual-beam charge neutralization. Core-level spectra were recorded with PHI SmartSoft VersaProbe (version 3.3.0) software and processed with PHI MultiPak (version 9.8). Sputter depth profiling was conducted using 1 keV Ar+ ions. Binding energies were referenced to the adventitious carbon signal at 284.8 eV. After subtraction of a Shirley-type background, the spectra were fitted with Gaussian–Lorentzian peak shapes.

Raman and photoluminescence. Raman and photoluminescence (PL) spectra were collected using Witec alpha 300R (Ulm, Germany) including a 100× objective lens (NA = 0.95) with a 532 nm excitation laser in the air under ambient conditions. The laser power was set at 200 μW for PL measurement to avoid laser heating and any other damage that the laser might produce. The spectrometer was calibrated to a specific frequency using a standard silicon wafer. For Raman measurements, spectral grating with 1800 lines/mm was used, whereas for PL, the spectral grating was 600 lines/mm.

Morphological observations. Stereomicroscopy illustrations were captured under white light conditions with a Keyence VHX-6000 (Osaka, Japan) microscope equipped with a 20–2000× objective, either under ring illumination or coaxial cross-polarized illumination. Images were recorded with different exposure times (high dynamic range—HDR) to achieve the best results. Furthermore, images were recorded in the x-y axis and stitched to a final panorama image with the help of the built-in software to overcome the field-of-view limitations. Before the file was saved, every single frame of the stitched image was focused. Thanks to that, we achieved an entirely sharp image detail.

Table 1 • Summary of material synthesis parameters of MoS_2 samples A, B, C, D, E, and F.

Sample	Method	Substrate	Sulfur precursor (phase)	Molybdenum precursor (phase)	Temperature (°C)	Pressure (mbar)	Duration (min)
A	MOCVD	c-sapphire	H_2S (gas)	$Mo(CO)_6$ (gas)	820	850	30
B	LqCVD	–	S (solid, 200 °C)	$(NH_4)_6Mo_7O_{24}$ (liquid)	700	800	15
C	Sulfurization	SiO_2	H_2S (gas)	Mo (solid)	–	–	–
D	CVD	SiO_2	–	–	750	0.9	–
E	–	–	–	–	–	–	–
F	CVD	SiO_2	MoS_2	MoS_2	950	0.3	–

In order to obtain the surface coverage of the as-grown MoS_2 films, center rectangular regions of the same size were cropped from the selected images for further processing. The chosen area was binarized first by converting it into an 8-bit format. Then, Otsu's method was used to perform automatic image thresholding. The algorithm returned a single intensity threshold that separated pixels into two classes: foreground and background. This threshold was determined by minimizing intra-class intensity variance or, equivalently, by maximizing inter-class variance. Each pixel in an image was replaced with a black or a white pixel. In the selected images (**Figure 1b**), this resulted in the lighter area that was not covered by MoS_2 flakes becoming completely black, and the MoS_2 flakes becoming completely white. Using this method, we easily calculated the total coverage of the selected area and the average size of a single MoS_2 flake.

TEM sample preparation. For the TEM experiments, all samples (A, B, E, and F) were directly supplied on TEM grids by the respective groups, who all used their own techniques for the transfer from the growth substrates. However, each group was supplied with holey carbon TEM grids from the same batch (Quantifoil Micro Tools GmbH, Germany). After the shipment, all TEM samples were stored under an Ar atmosphere to prevent sample degradation. Before TEM investigation, a pre-characterization of the TEM samples was conducted with a light microscope in reflection mode, to identify suitable sample regions for the TEM experiments. Immediately before the samples were loaded in the TEM, they were annealed for 25 min. at 200 °C, in order to reduce the amount of hydrocarbon on the samples. The TEM experiments were then performed in a high vacuum ($\sim 10^{-5}$ Pa), without in situ cooling or heating of the samples.

Electron diffraction. During the TEM experiments, monolayers of MoS_2 were first identified by selected-area electron diffraction (SAED), using the intensity differences among the first-order Bragg reflections as a clear indication for the MoS_2 monolayer [27]. Over large sample areas (with diameters of approx. 0.1–1 μm), SAED also allowed for discrimination between single-crystalline and monocrystalline MoS_2. The grain boundaries in polycrystalline MoS_2 could be easily recognized based on the presence of multiple sets of first-order Bragg reflections. An exemplary SAED pattern of monolayer MoS_2 is shown in Section 6.1. of the Supplementary materials.

High-resolution TEM. Aberration-corrected high-resolution TEM (AC-HRTEM) imaging was performed in the SALVE (Sub-Ångstrom Low-Voltage Electron Microscopy) TEM [28] with correction for the spherical and chromatic aberration (C_s & C_c). A low acceleration of 60 kV was used to minimize electron beam-induced damage during imaging. The HRTEM imaging conditions were optimized for bright-atom contrast using a small negative C_s. Due to C_c correction, the instrumental resolution was better than 1 Å. All HRTEM images were recorded with an FEI / Thermo Fisher Ceta CMOS camera with 4096×4096 pixels.

Device fabrication for C-V experiments. A metal-insulator-semiconductor (MIS) capacitor based on (MO)CVD-grown MoS_2 was fabricated according to the following steps to obtain the capacitance voltage (C-V) measurements. The bottom gate was patterned on sapphire substrate by photolithography, followed by Ti/Au deposition using an e-beam evaporator. The insulating layer was 30 nm hafnium oxide (HfO_2) grown by atomic layer deposition (ALD). The identical substrates patterned according to the above steps (Figure S25) were then delivered to our partners for MoS_2 transfer. Afterwards, the transferred chips were sent back for the remainder of the device fabrication and measurement. Samples which were returned were then annealed in Ar/H_2 atmosphere to remove possible polymer residues and surface contamination. Atomic force microscopy was performed on each chip to check the cleanness and completeness of the flake. The top contact was then patterned by e-beam lithography, and deposited with 2 nm Ti and 80 nm Au contact by e-beam evaporation. For continuous film sample, O_2 plasma etching was performed before contact deposition to remove extra materials and leave only a few hundreds μm^2 of materials for further measurement. The final MIS device structure for C-V measurements is shown in Figure S26a,b, where MoS_2 crystal is only contacted by a narrow region at the edge.

C-V measurement. Before performing the C-V measurement, the devices were first annealed in a high-vacuum (10^{-6} mbar) tube furnace at 200 °C for 3 h to reduce the contact resistance, followed by an in situ annealing at 140 °C overnight to remove the moisture and adsorbate from the surface. C-V measurement was then performed by applying a DC bias between the bottom gate and the top contact, in combination with a 50 mV AC signal with frequency changing from 1 kHz to 1 MHz. Figure S26 shows the

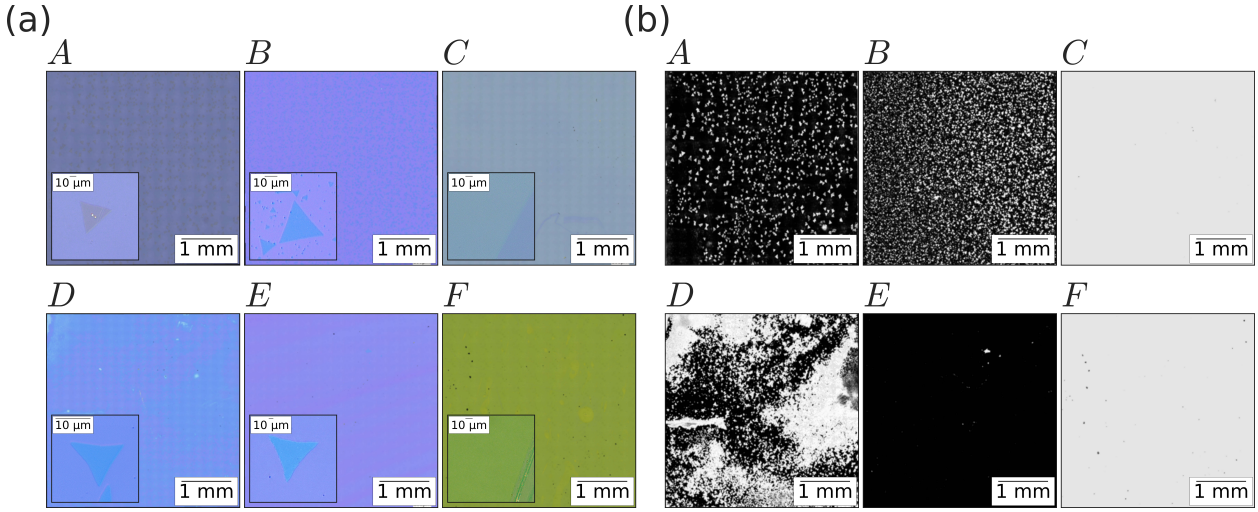


Figure 1 • (**a**) Optical microscopy images of samples A, B, C, D, E, and F on a growth substrate, with insets outlining single flakes or scratches that reveal differences between the film and the substrate. (**b**) Binarized optical images of CVD MoS_2 allowing us to better analyze the surface coverage of samples A, B, C, D, E, and F. White region representing MoS_2 coverage.

result of frequency dependent C-V measurement on a single-crystal MoS_2 device Figure S26b). Since MoS_2 is naturally an n-type semiconductor, tuning the gate voltage allows electrical control between depletion and accumulation regions, allowing gradual trap states to be filled and emptied, thus showing up in the transition region in the C-V curve. Numerical calculations using the band-tail DOS model were performed with a Matlab code, where α and φ values were obtained by fitting the model to the experimental C-V curves at 1 kHz frequency.

Sample fabrication. Sample A: The metal–organic chemical vapor deposition (MOCVD) method was used to synthesize sample A, where the two gas-phase precursors (molybdenum hexacarbonyl, $Mo(CO)_6$, and hydrogen sulfide, H_2S) were mixed with a flow rate ratio of 1:6028 in a 2-inch MOCVD furnace. To promote large-area epitaxy growth, atomically smooth sapphire was used as the substrate, which was first annealed at 1000 °C in air [29] and then spin-coated with NaCl solution before the growth [30]. The reaction took place at 820 °C in an Ar atmosphere and lasted for 30 min, while the $Mo(CO)_6$ bubbler was heated at 15 °C. Afterward, the furnace underwent a slow cooling process to 150 °C with continuous Ar and H_2S flow. Throughout the process, the furnace pressure was controlled to be 850 mbar.

Sample B: For the growth of MoS_2 flakes, the liquid-phase chemical vapor deposition (LqCVD) growth method was used. Firstly, two aqueous solutions (solution A and solution B) containing ammonium heptamolybdate, as Mo precursor, and NaOH, as growth promoter, were prepared by dissolving 0.4 g of AHM in 30 mL deionized (DI) water and 0.1 g of NaOH in 40 mL of DI water, respectively. After this, solution A, solution B, and iodixanol were mixed using a solutions ratio of 1:1.5:1 and then spin-coated on the substrate. Finally, the growth was carried out in a two-zone horizontal furnace, where the spin-coated substrate was heated at 700 °C in atmospheric pressure (800 mbar) for 15 min under constant Ar flux, while sulfur was maintained at 200 °C

Sample C: First, we deposited a thin layer of Molybdenum on 2-inch SiO_2 substrates. It was carried out in e-beam evaporation in Kurt Lesker PVD system under 5×10^{-7} Thor pressure. The deposition rate was maintained at a very low level, and samples were mounted on a rotating disc. After that, sputtered samples with a Mo layer were placed in a CVD reactor for sulfurization to form MoS_2 film. H_2S was used as the precursor of sulfur and H_2 was used as the carrier gas.

Sample D: The MoS_2 flakes were synthesized on 290 nm SiO_2/Si in a two-zone CVD furnace using a microcavity reactor as Mo precursor supply. The growth temperature was 750 °C with a pressure of 0.9 mbar.

Sample E: The MoS_2 flakes were synthesized on 285 nm SiO_2/Si in a two-zone CVD furnace using MoS_2 powder as a precursor supply. The growth temperature was 800 °C with a pressure of 133.322 mbar.

Sample F: The MoS_2 flakes were synthesized on 300 nm SiO_2/Si in a single-zone CVD furnace using MoS_2 powder as a precursor supply. The growth temperature was 950 °C with a pressure of 0.3 mbar.

Detailed information about the sample fabrication and growth parameters can be found in Supplementary materials (Subsection 7.1).

3. Results

3.1. Optical characterization

Figure 1a displays optical microscope images of six MoS_2 samples that were grown using CVD by various research groups. More comprehensive information on these samples can be found in Section 1 of the Supplementary materials.

Based on optical microscopy, sample morphologies were identified and are described in detail in **Table 2** and Table S1. The surface coverage differs from sample to sample in the range of 0.11% to 99.98% Among them, samples A, B, and E are isolated MoS_2 flakes with triangular shapes, sample C and F are polycrystalline MoS_2 films, and sample D is composed of connected MoS_2 pockets of triangles.

It should be emphasized that the choice of method for counting the particles can significantly impact the results, particularly when clusters of flakes are present (as seen in **Figure 1b**, D). As a result, the counts reported in Table S1 may be prone to errors. Therefore, the most reliable indicator in this case is the total coverage area, which can be found in Figure S1.

Additionally, the MoS_2 samples were transferred onto a sapphire substrate, and intactness of their morphology was examined using an optical microscope. Upon transfer, visible cracks in the samples were observed, along with polymer residues that were detected through atomic force microscopy. The details of these observations can be found in Supplementary materials Section 1.

3.2. Raman characterization

As illustrated in **Figure 2a** the Raman spectrum of MoS_2 when excited with 532-nm laser light exhibits two characteristic peaks around 383 and 408 cm^{-1} which corresponds to the in-plane E^1_{2g} mode and out-of-plane A_{1g} mode, respectively.

The position of the E^12g band shifts gradually from 32 cm^{-1} for the bulk to 23 cm^{-1} for the single trilayer [31]. Additionally, the band positions and separations of the E^12g and A_{1g} bands show systematic changes between the bulk and a single layer. An example of such spectrum evolution of MoS_2 from bulk material to a monolayer (1L) is shown in Li et al. [32]. For instance, the E^12g band (383 cm^{-1}) shifts to a higher wavenumber, and the $A1g$ band (408 cm^{-1}) shifts to a lower wavenumber as the material thickness decreases from bulk to monolayer, leading to a band separation that changes from 25 cm^{-1} to 19 cm^{-1}, respectively. These shifts in the Raman band positions, particularly the frequency difference between the E^12g and $A1g$ modes, are most readily observed when using a wavelength excitation of 532 nm or shorter.

In CVD-grown materials, there have been reports of a more substantial separation between the two peaks in the Raman spectrum, which is often attributed to strain or doping in the deposited films, according to the literature [33]. Additionally, manually applied disturbances, unintentional substrate effects [34], and environmental effects can cause dielectric or doping changes that result in a shift in Raman peaks. These effects typically coincide, so caution should be exercised when interpreting changes in the Raman spectra.

Figure 2a displays six typical Raman spectra obtained from various CVD-grown MoS_2 samples. Large-scale Raman maps were obtained for all samples under the same ambient conditions to

Table 2 • Measured Properties of Samples Using Analytical Techniques.

	Method	Sample A	Sample B	Sample C	Sample D	Sample E	Sample F
Morphology	Optical Microscopy	Small triangular flakes	Small triangular flakes	Polycrystalline	Connected large pockets	One large flake surrounded by a few smaller ones	Polycrystalline
Surface coverage [%]	Optical Microscopy	8.53	23.84	99.97	53.13	0.11	99.98
Intensity ratio (E^1_{2g}/A_{1g})	Raman Spectroscopy	1.30 ± 1.06	0.93 ± 0.23	0.74 ± 0.19	0.94 ± 0.43	0.99 ± 0.23	0.80 ± 0.90
Position of E^1_{2g} [cm^{-1}]	Raman Spectroscopy	385.55 ± 1.40	384.49 ± 0.31	384.74 ± 2.58	384.91 ± 1.53	388.22 ± 0.51	385.23 ± 0.95
Position of A_{1g} [cm^{-1}]	Raman Spectroscopy	407.03 ± 2.78	404.37 ± 0.36	408.96 ± 1.07	407.08 ± 0.89	405.08 ± 0.61	407.13 ± 0.68
Position of A-exciton [eV]	PL	1.8008 ± 0.0066	1.8411 ± 0.0254	1.8715 ± 0.0844	1.8341 ± 0.0082	1.8521 ± 0.0087	1.8494 ± 0.0149
S 2s [%]	XPS	–	55.83	57.97	53.25	59.13	57.40
MoS_2 [%]	XPS	–	34.97	30.17	30.17	38.92	33.60
MoO_3 [%]	XPS	–	9.20	11.86	12.93	1.95	9.00
Defect density C_0 [vac./nm^2]	TEM	0.10 ± 0.04	0.40 ± 0.05	–	–	0.16 ± 0.06	0.14 ± 0.05
Integrated DOS (10^{14} cm^{-2})	CV	4.08	4.28	–	–	4.14	4.15

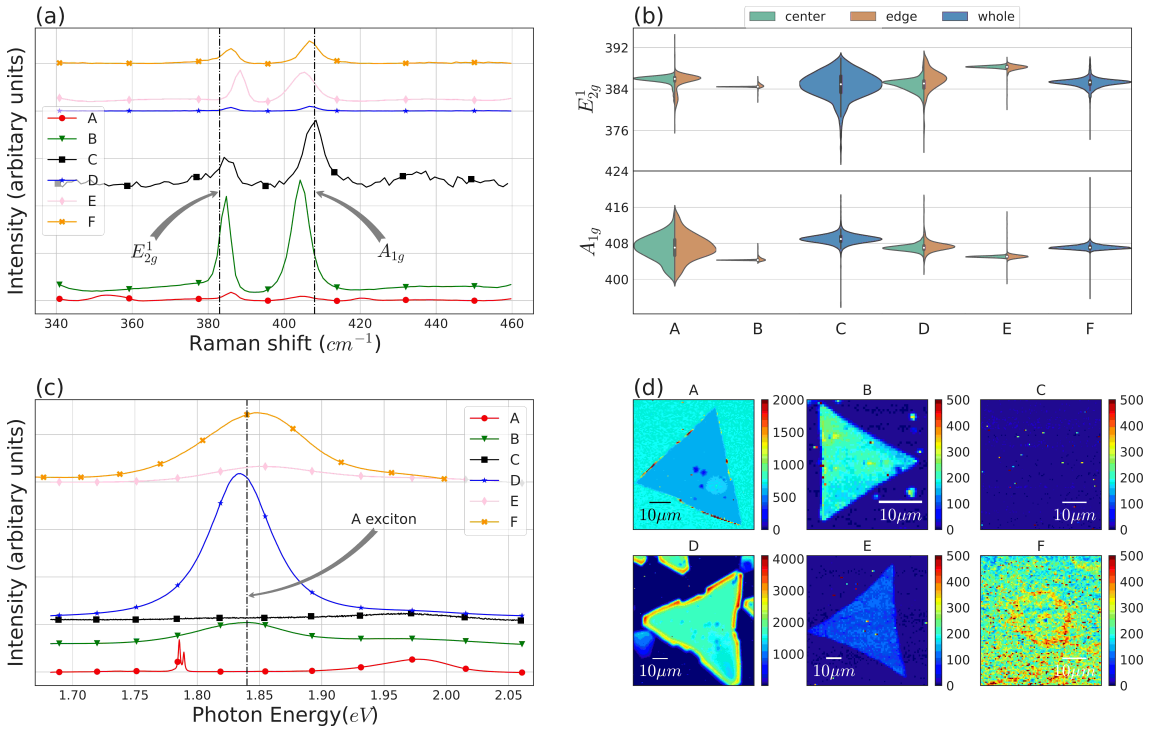


Figure 2 • (**a**) Typical Raman spectra of CVD MoS_2 collected with a 532 nm excitation wavelength from samples A to F, respectively. Spectra are offset vertically for clarity. (**b**) Violin plots of E^1_{2g} and A_{1g} modes collected from samples A to F. Red- and green-shaded colors correspond to the flake's edge and a center region. (**c**) Exemplary photoluminescence spectra of CVD MoS_2 collected from samples A to F, respectively, before transfer. Spectra are offset vertically for clarity (**d**) Photoluminescence maps of *A* excitons collected from samples A to F, respectively, with a 532 nm excitation wavelength. Blue and red colors correspond to low and high intensities, respectively.

observe the shift of Raman modes within a flake as accurately as possible. The Raman setup's basic parameters are presented in Table S2. The mapping was consistently established to encompass a complete flake. The spectra obtained with 532 nm excitation are typical of those commonly reported in the literature. Both the E^1_{2g} mode (Figure S3) and the A_{1g} mode (Figure S4) originating from MoS_2 are present, along with the characteristic silicone peak (substrate) at 520 cm^{-1}, as expected.

The peak intensities of E^1_{2g} and A_{1g} modes for the samples (Figure S3) were measured and studied as an indicator of material uniformity. Background subtraction was performed the same way for all samples to ensure fair comparisons among them and this resulted in intensities between 40 and 100.

The intensity of E^1_{2g} mode for samples B and F leads to uniform Raman responses throughout, as expected for homogeneous films. Sample C (film) projects a high variation in Raman intensity and low crystallinity. Flakes on samples D and E flakes appear grainy, suggesting inter-flake composition variations. Additionally, pronounced intensity discrepancy between the basal plane and the edge of the flake can be observed, and it is the strongest for samples A and E.

A similar characteristic can also be observed in the case of A_{1g} peak (Figure S4). Here, arbitrary intensity across the samples after background subtraction was between 40 and 400. Samples A, B, and F are internally relatively uniform. Flakes D and E are grainy, and C has a high signal variation. Sample E also exhibits minimal difference in intensity between the basal plane and the edge. However, it is reported that the A_{1g} phonon mode is preferentially excited for edge-terminated surfaces, resulting in much higher intensity in the A_{1g} peak compared to the E^1_{2g} peak and Raman intensities rising from one to two layers of MoS_2.

Figure S4 and Table S3 indicate the positions of E^1_{2g} and A_{1g} modes, respectively, for each sample. In the case of E^1_{2g} mode, it appears at the lowest wave number for sample B (center) 384.44 ± 0.05 and the highest for sample E (center) 388.32 ± 0.21. Likewise, A_{1g} shows up at the lowest wavenumber for the sample B (center) 404.28 ± 0.06 and the highest value belongs to sample C (whole) 408.96 ± 1.07. **Figure 2b** displays violin plots of the distributions of E^1_{2g} and A_{1g} Raman band intensities of MoS_2 for different samples. Violin plots are similar to box plots, except that they also show the probability density of the data at different values. The white dots in Figure 2b indicate the median, allowing quick comparisons of average peak positions among multiple data samples. The black bars indicate the first and third quartiles (interquartile range). The 'whiskers' extend to points within 1.5 IQRs of the lower and upper quartile, and observations that fall outside this range are considered outliers. This means that each value in the Figure 2b corresponds to an actual observation in the Raman peak positions. The surrounding violin shell consists of a local kernel density estimation (KDE) for the center (left) and edge (right) of the sample and, in the case of C and F, mirrored KDE for the whole piece. KDE graphically shows the distributional characteristics of Raman peak positions within each sample. These results are in line with earlier observations noted by Zhangting Wu et al. [35], Zhong Lin et al. [36], and Dan Wang et al. [37].

Similar observations of Raman modes were acquired after the transfer of MoS_2 to sapphire substrates for all available samples under the same ambient conditions. The results of that analysis are presented in Supplementary materials Subsection 2.2.

3.3. Photoluminescence characterization

The absorption spectrum of MoS_2 typically shows a fine structure with narrow absorption peaks positioned according to the literature at around 1.84 eV (674 nm, 14841 cm^{-1}) and 2.01 eV (616 nm, 16,234 cm^{-1}). Both are related to d-to-d orbital transitions split by spin–orbit coupling and designated A and B excitons, respectively. It is shown that the A exciton peak of monolayer MoS_2 is actually a combination of the neutral exciton (A^0) and trion (A^-) emission peaks, where A^- peaks were situated ≈ 35 meV lower than the A^0 peak. An important advantage of MoS_2 spectroscopy is that one can obtain a photoluminescence (PL) spectrum simultaneously with Raman.

An exemplary effect of excitation wavelength on the PL spectra of the six samples of MoS_2 can be seen in **Figure 2c**. The basic parameters of the PL setup are presented in Table S5. The arbitrary intensity of A exciton for the samples (**Figure 2d**) across all the samples after background subtraction was between 500 and 4000. Higher PL intensity means a higher quantum yield, indicating low defect density and allowing easier electron recombination. Sample A is grown on top of sapphire, and the others are grown on SiO_2/Si substrate. Sample A flake appears to have less photoluminescence intensity than the background, most likely due to the quenching effect of the sapphire substrate. Samples B and E exhibit uniform photoluminescence responses throughout the flake. Sample C (film) projects a meager response. As noted earlier, the structure of few-layer MoS_2 films usually varies spatially, and the most notable changes appear at the edges. This is most clearly visible in the case of sample D in **Figure 2d**. Sample F (film) has a locally high response, but it also presents the most significant variation in signal. Detailed parameters like the positions of A-exciton or FWHM can be found in Table S4.

Similar observations of the photoluminescence spectra of six MoS_2 samples after transfer to the new substrate and their analysis can be seen in the Supplementary materials Subsection 3.2.

3.4. X-ray photoelectron spectroscopy characterization

The chemical composition of the CVD-grown MoS_2 samples is further studied using X-ray photoelectron spectroscopy [38]. XPS is a highly sensitive surface-based technique, as the X-ray-generated photoelectrons steam the outermost layers, typically penetrating only a few nanometers. Thus, it is an ideal instrument for characterizing 2D materials. As shown in the XPS spectra (**Figure 3a** and Figure S14), five major bands representing chemical states appear with binding energies ranging from 220 eV to 250 eV. They represent the MoS_2 (Mo^{4+}) doublet, the MoO_3 (Mo^{6+}) doublet, and the S 2*s* singlet, respectively. As indicated in previous reports [39], careful evaluation of the deconvoluted XPS spectral features (peak position, full-width half-maximum (FWHM), peak intensity, or integrated area) allow us to estimate the degree of crystalline disorder and stoichiometric ratios of MoS_2 samples.

Therefore, we perform the exact XPS measurement on all samples. The obtained results are listed in Supplementary materials Section 4 and plotted in **Figure 3c–e**. The binding energies extracted for samples are well aligned with the reference value (indicated by the dashed line in **Figure 3c**), with slight variation among different samples as well as between pristine and transferred samples. One obvious exception is sample C, where the Mo^{4+} (or MoS_2) doublet peaks exhibit 1 eV lower binding energy (**Figure 3c**)

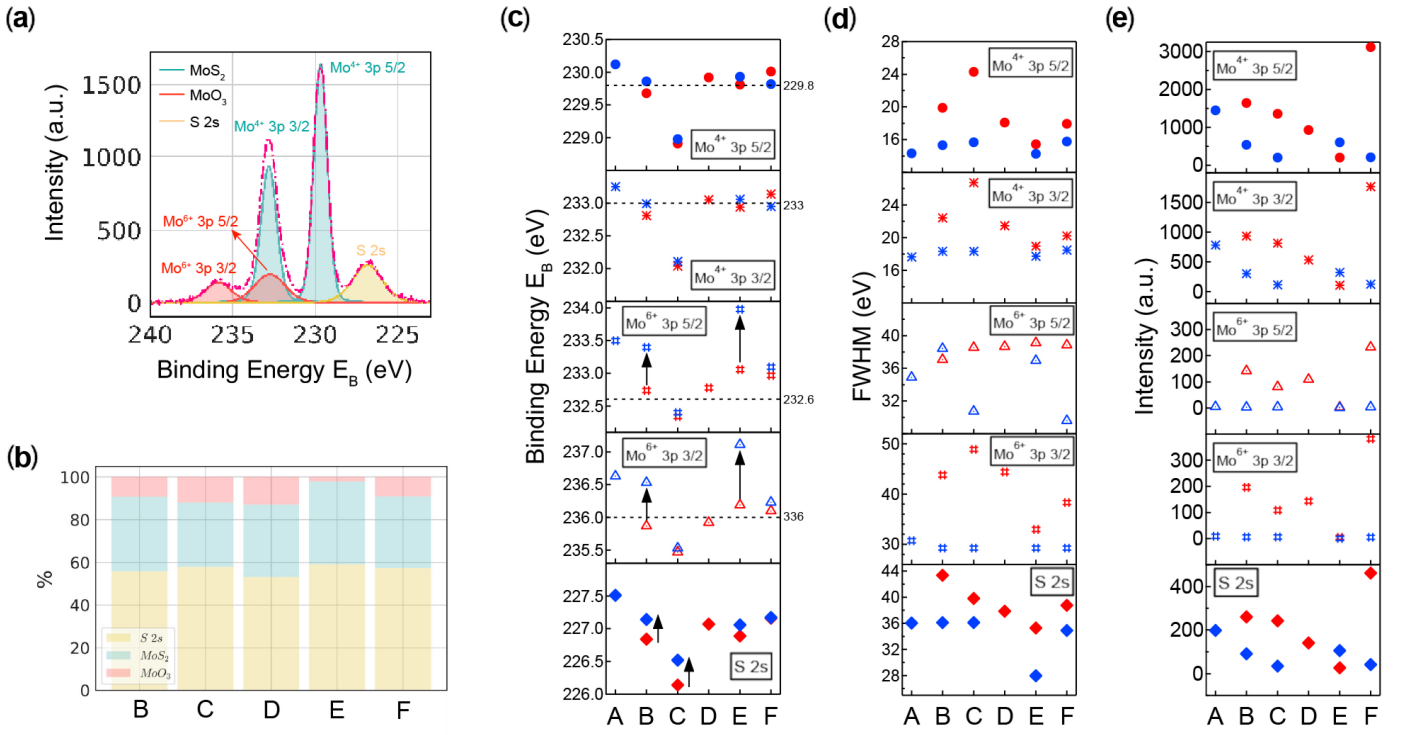


Figure 3 • X-ray photoelectron spectroscopy results. (**a**) An example of XPS spectra of MoS_2 fitted with five peaks. (**b**) Percentage ratio for each MoS_2 sample. (**c**) Binding energy. (**d**) FWHM. (**e**) Intensity of each peak. The red and blue markers in (**b**–**e**) represent values before and after the transfer.

and significantly higher FWHM values (**Figure 3d**) compared to other samples, indicating a very defective/substoichiometric MoS_2 sample composition with an excessively high amount of sulfur vacancies. In addition, sample A demonstrates slightly higher (0.3 eV) binding energies and a smaller FWHM for Mo^{4+} doublet and S 2*s* singlet, indicating a comparably higher material quality. Other samples, including B, D, E, and F, demonstrate comparable material quality, as revealed by the similar level of binding energies and FWHM.

After the material transfer from as-grown sapphire or SiO_2 substrate, a significant EB increase (1 eV) of Mo^{6+} (or MoO_3) doublet is observed for samples B and E, indicating oxidation. The FWHM and peak intensity are noticeably reduced after the transfer.

To better compare the chemical composition of each chemical species, **Figure 3b** plot the percentage factor of the three components: Mo^{4+} (MoS_2), Mo^{6+} (MoO_3), and S 2*s*. Apparently, sample E contains the smallest amount of MoO_3, indicating a low oxidation level and high MoS_2 purity. Sample B, C, D, and F contain a similar amount of MoO_3, but the Mo/S ratios vary.

3.5. Transmission electron microscopy characterization

Using transmission electron microscopy (TEM), a total of four different samples (A, B, E, F) of freestanding CVD MoS_2 were analyzed with respect to their atomic structure. In particular, their intrinsic defect densities were determined by directly counting sulfur vacancies in a series of atomically resolved C_c/C_s-corrected high-resolution TEM (HRTEM) images of clean, single-crystalline areas. This technique has already been described by Shreeet et al. [40] and George et al. [4] and extrapolates the density of intrinsic defects (sulfur vacancies) from the linearly increasing number of defects under electron irradiation. Our direct results from this method are summarized in **Figure 4**, which shows an exemplary HRTEM image (**Figure 4a,b**) along with a plot of the beam-induced evolution of the defect densities in all four samples (**Figure 4c**).

Each data point in **Figure 4c** was obtained by counting the sulfur vacancies in a single HRTEM image of a 723–1590 nm^2 large, clean MoS_2 area. The counting of these defects was facilitated by removing the regular MoS_2 lattice by a Fourier filter (cf. **Figure 4a,b**). In the course of the HRTEM image series, we observed that the combined density of single and double sulfur vacancies increased linearly with the applied electron dose, corresponding to a stochastic creation of new defects. Using linear regressions (solid, dashed, dotted, and dashed–dotted lines), the intrinsic defect densities C_0 at the beginning of the TEM experiments could finally be determined based on the *y*-intercepts in the plot. **Table 3** gives an overview of these intrinsic defect densities, along with the investigated sample areas *A* and the rates of the sulfur vacancy formation *C*. For these values, it has to be noted that the rate of defect creation in the polycrystalline sample F was more than five times higher than for the other investigated samples. The electron dose rate during this TEM experiment had to be significantly reduced for the defect creation to happen on an appropriate timescale of several minutes (cf. Figure S19 of the Supplementary materials). This can most likely be attributed to higher contamination of this TEM sample or lower vacuum conditions, which accelerated the defect formation. However, in most cases, the rate of defect formation *C* should not affect the number of *intrinsic* defects C_0. Further information on the evaluation of the different samples and the assumed measurement errors can be found in the Supplementary materials (Subsection 6.2).

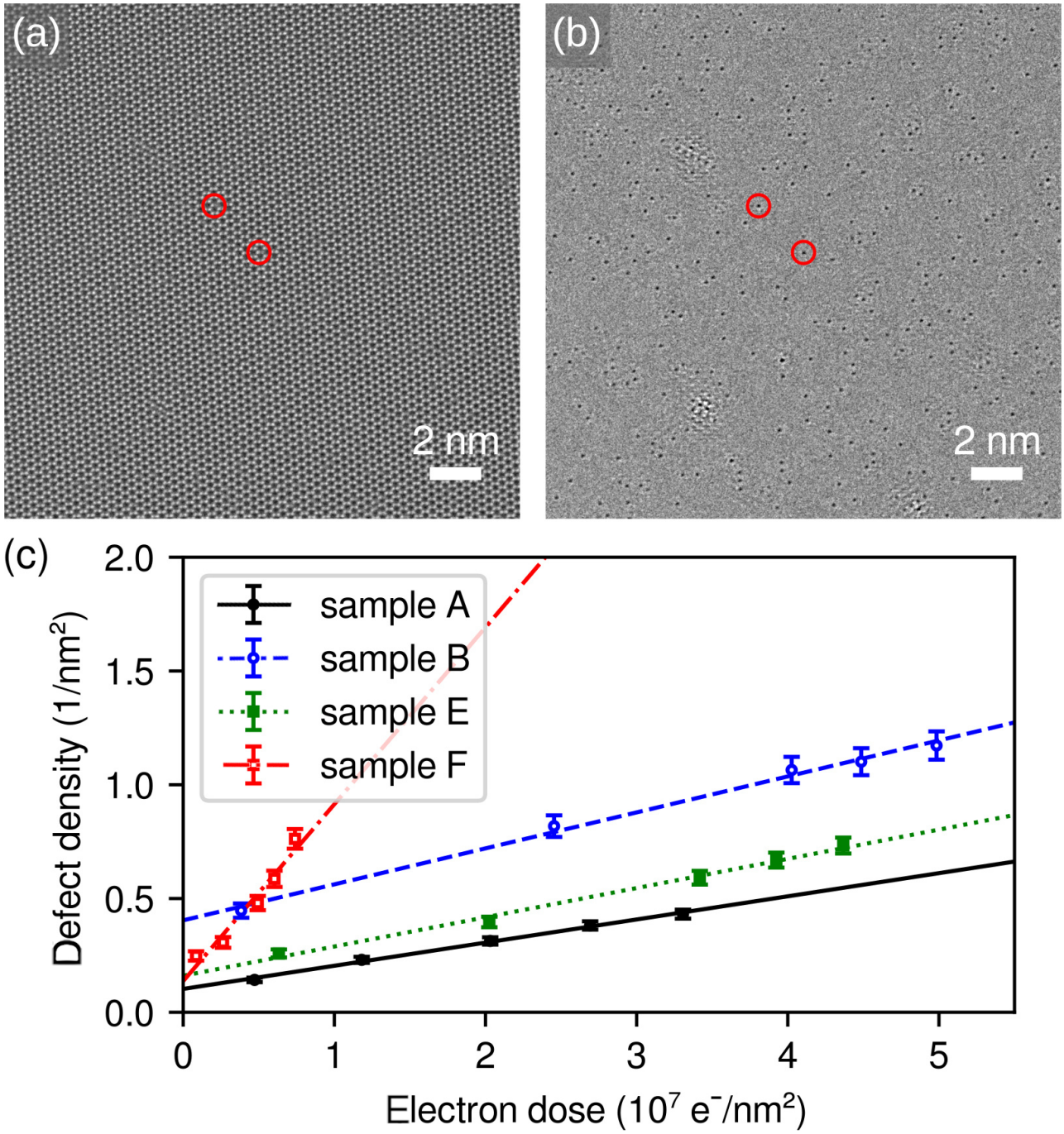


Figure 4 • Determination of intrinsic defect densities by low-voltage HRTEM at 60 kV: (**a**) Exemplary C_c/C_s-corrected HRTEM image of CVD MoS_2 (sample A, SC, MOCVD) with intrinsic and electron beam-induced sulfur vacancies. Red circles mark two sulfur vacancies. (**b**) Fourier-filtered version of the same image where the regular MoS_2 lattice was removed for easier recognition of vacancies (dark spots). (**c**) Evolution of defect densities under electron irradiation for samples A (black solid line), B (blue dashed line), E (green dotted line), and F (red dash-dotted line). The defect densities were determined from the Fourier-filtered HRTEM image series.

Table 3 • Defect evolution in HRTEM of MoS_2 samples A, B, E, and F: Investigated area A, rate of the sulfur vacancy formation C, and density of intrinsic defects C_0.

Sample	A (nm^2)	C (vac./e$^-$)	C_0 (vac./nm^2)
A	1590 ± 40	$(10.2 \pm 1.8) \cdot 10^{-9}$	0.10 ± 0.04
B	660 ± 26	$(15.8 \pm 1.7) \cdot 10^{-9}$	0.40 ± 0.05
E	1030 ± 40	$(12.8 \pm 2.3) \cdot 10^{-9}$	0.16 ± 0.06
F	723 ± 27	$(78 \pm 12) \cdot 10^{-9}$	0.14 ± 0.05

Eventually, the determination of defect densities by HRTEM yielded the following results for the investigated samples A, B, E, and F: The monocrystalline triangular MoS_2 flakes of sample A had the lowest density of intrinsic defects, with only (0.10 ± 0.04) sulfur vacancies per nm^2. Surprisingly, the second-lowest defect density was determined for a very different sample. The polycrystalline sample F with very high coverage also had only (0.14 ± 0.05) vacancies per nm^2, closely followed by another sample with individual triangular flakes [sample E, (0.16 ± 0.06) vac./nm^2]. By contrast, sample B with individual triangular flakes had a significantly higher density of intrinsic defects with (0.40 ± 0.05) vac./nm^2. From these results, we can conclude that no general

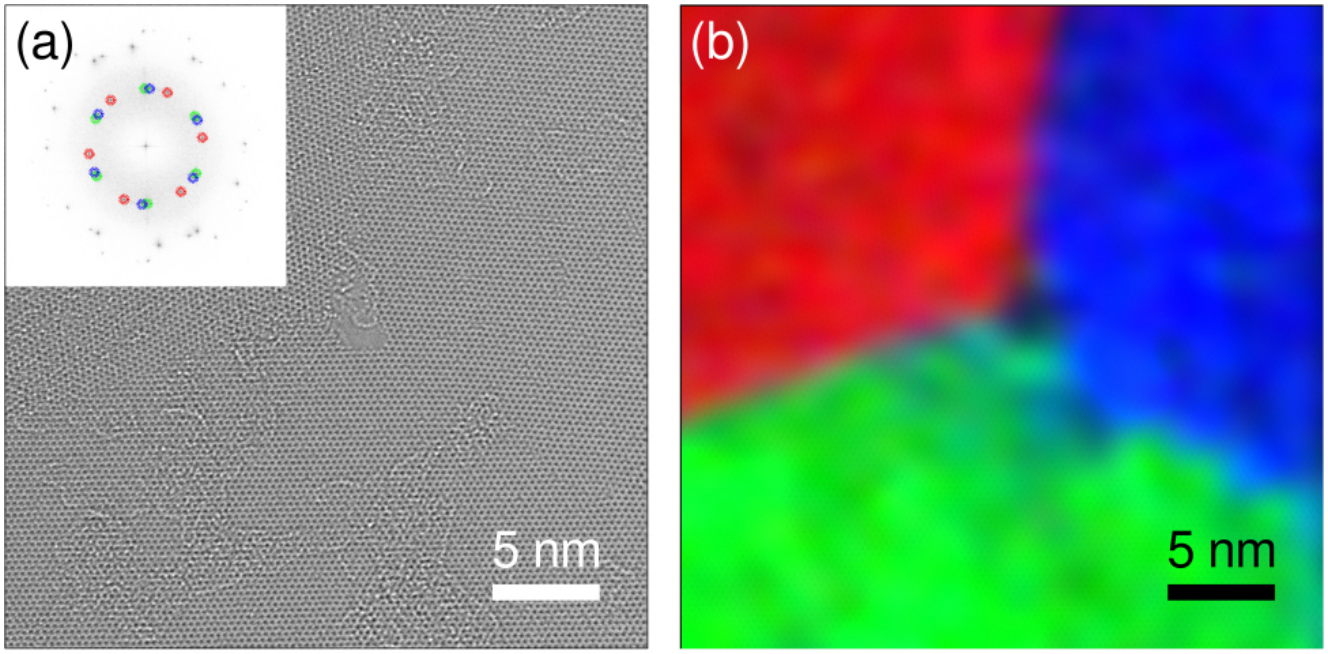


Figure 5 • TEM of MoS_2 grain boundaries and multilayers: (**a**) C_c/C_s-corrected 60 kV HRTEM image of grain boundaries in sample F. In the FFT inset, red, green, and blue circles are marked by three sets of $\{10\bar{1}0\}$ Bragg reflections belonging to the different grains. (**b**) Map of the grain orientations in (**a**) with the same color coding.

connection was found between the morphology and defect density of the samples of the CVD MoS_2. In addition to their grain boundaries, polycrystalline MoS_2 films can have similar defect densities to individual monocrystalline flakes.

In the context of the HRTEM experiments, however, we also have to emphasize the role of the cleanliness of the TEM samples. Sample A was the cleanest sample, as seen from the large investigated area of 1590 nm^2 that was completely contamination-free. This allowed for very clear imaging of the MoS_2 lattice at the atomic resolution and made the sample more robust against electron beam-induced damage. With a rate of only $(10.2\pm1.8)\cdot10^{-9}$ created sulfur vacancies per primary electron, this was the most stable of all the samples. Most of the stronger contamination on the other samples came from the transfer of the MoS_2 to the TEM grid and was not present on the as-grown CVD MoS_2. This is an example of how the transfer of 2D materials can strongly affect their properties and shows the importance of clean transfer methods.

In addition to determining the intrinsic defect densities, HRTEM imaging was also used to analyze the samples' grain boundaries and multilayer areas. While grain boundaries can be easily observed in MoS_2 samples with nearly complete coverage, samples with isolated single-crystalline flakes, in some cases, featured multilayer areas, with one or more additional layers grown on top of the monolayer MoS_2. In **Figure 5**, these two cases are illustrated by HRTEM images from samples F (high coverage) and A (low coverage). **Figure 5a** depicts a raw HRTEM image of grain boundaries in sample F, along with the fast Fourier transform (FFT) of the image (inset, contrast inverted). As marked by the red, green, and blue circles, the FFT shows Bragg reflections from MoS_2 grains in three distinct orientations. Using the same color-coding, **Figure 5b** directly shows the areas of the three grains within the image via an orientation mapping technique based on Fourier filtering [41].

3.6. Capacitance–voltage (C-V) characterization

Capacitance–voltage (C-V) measurement is adopted to estimate the density of in-gap states created by point defects such as sulfur vacancies [42]. In order to achieve superior gate control and low surface roughness, we utilized a metal-insulator-semiconductor (MIS) capacitor configuration (**Figure 6a**) based on the (MO)CVD-grown MoS_2 crystals, 30 nm thick high-quality hafnium oxide (HfO_2), and a 2/30 nm Cr/Au back gate. In addition, sapphire was used as the device substrate to eliminate parasite capacitance from the background. Au was deposited at the edge of MoS_2 crystals to serve as an ohmic contact for effective charge injection. During the C-V measurement, a varied DC bias was applied between the bottom gate and the top contact, in combination with a 50 mV AC signal with frequency changing from 1 kHz to 1 MHz (**Figure 6a**). The typical C-V curves measured under different frequencies are shown in **Figure 6c**. The apparent capacitance increase at around 0.3 V indicates the n-type conductivity of sample A. At low oscillation frequencies, the capacitance increases expeditiously with the gate voltage V_G. At high frequencies, the carrier response is much slower, indicating the existence of slow trap states at the conduction band edge, which is created by various crystal defects or interface imperfections.

The sulfur vacancy defects observed from HRTEM (**Figure 4**) are known to create a trap state very close to the conduction band minimum [43]. Therefore, the material quality can be sensitively detected and reflected on the transition part of the C-V curves. When solving the electrostatic condition of the MIS device (Figure S27), we utilize a band-tail density-of-state (DOS) model (**Figure 6d**) to calculate the carrier concentration and estimate the trap-induced states quantitatively [42, 44]. It is composed of two parts: the trap states located inside the bandgap close to the band edge, and the intrinsic density of states of MoS_2 conduction band, as expressed

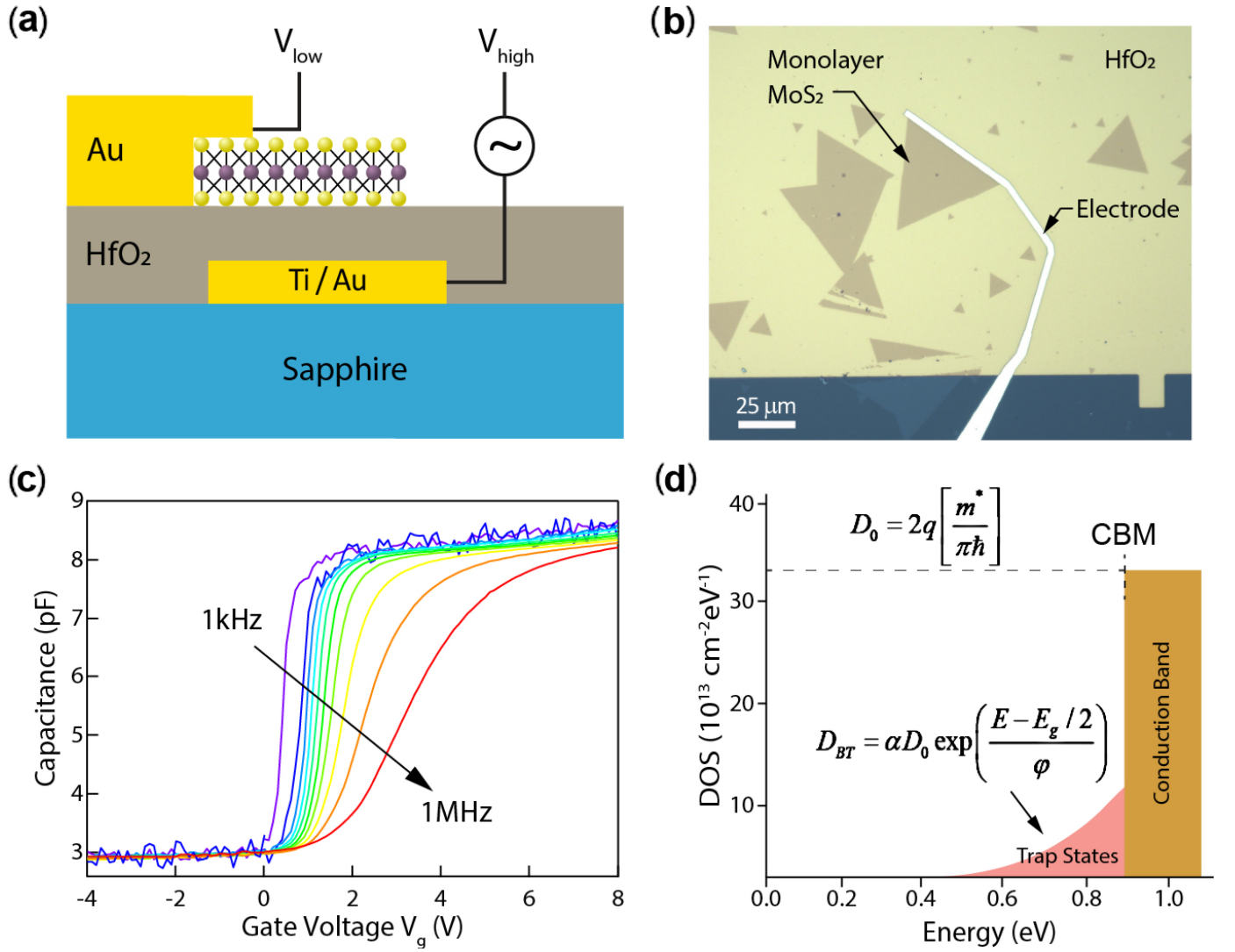


Figure 6 • Metal insulator semiconductor (MIS) configurations for capacitance–voltage measurement. (**a**) Device schematics for the MoS_2 capacitor. (**b**) Optical image of a device for C-V measurements, including sample A (MOCVD-MoS_2) as the channel material. (**c**) Dependence of device capacitance as a function of voltage measured for different excitation frequencies. (**d**) Density of state diagram of MoS_2 band edge trap states, taken from [44]. In panel b-c, sample A is used as an example to demonstrate the C-V configurations. More device pictures and measurement results are shown in Supplementary materials Section 7.

with a piece-wise formula in Equation (1)

$$D(E) = \begin{cases} D_0 = 2 \cdot (\frac{m^*}{\pi \cdot \hbar^2}) & E \geq E_C \\ \alpha \cdot D_0 \cdot exp(\frac{E-E_C}{\phi}) & E < E_C \end{cases} \quad (1)$$

The characteristic of band-tail traps and defects can be quantified using α and ϕ values in the DOS model, defining the density and extent of the defects inside the bandgap. To quantify the concentration and energy level of defects in (MO)CVD-grown MoS_2, a numerical simulation is performed to fit the theoretical capacitance to the experimental data by changing the α and ϕ values.

We performed the same measurement and fittings on MIS devices based on Sample A, B, E, and F, and at least five devices were measured for each type of material to eliminate any random errors. The C-V curves and fittings for all the devices are shown in Supplementary materials Section 7, and the statistic evaluations for the α and ϕ values are listed in Table S10 and plotted in **Figure 7a**. Sample A has the lowest ϕ value ($\sim$ 80 meV), indicating the shallowest trap state distribution at the band edge. In contrast, samples E, F, and B have wider extensions ($\sim$ 160 meV), resulting in threshold shift and increased off-current. In comparison, the α values for different samples are almost similar, except for sample B, which shows a higher α value. By inputting these values into the DOS model, we can obtain the energy spreading for each sample. Sample A demonstrates the lowest trap density, which only spreads lightly at the bent edge, while samples B, E, and F exhibit larger defect densities and deeper energy extension.

4. Discussion

Even though the exact definition of TMD quality remains unclear, the advanced characterization techniques mentioned in this text can be used to identify several parameters for evaluating the quality of produced films. However, it should be noted that some of these methods are destructive and require specific sample preparation, such as transfer onto appropriate substrates, which can change the material's properties. Additionally, some techniques are subjective and do not allow continuous monitoring, as they can only be used for a final evaluation.

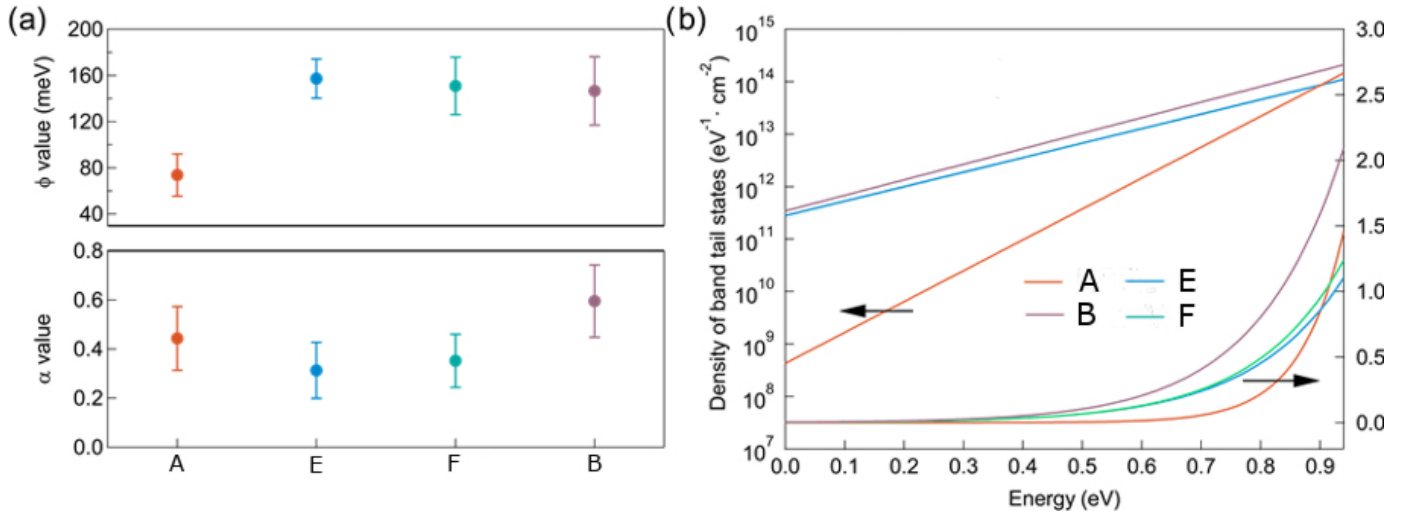


Figure 7 • Quantitative analysis of defect-induced band edge states by C-V measurement. (**a**) α and ϕ values extracted from the C-V fittings for different samples. (**b**) Density of band tail states distribution as a function of energy ranging from mid gap to the conduction band edge. The left and right axis correspond to logarithm and linear coordinates, respectively. The higher value of band tail states means a larger defect concentration in the MoS_2 sample.

Optical microscopy is a low-cost, non-destructive method that drastically reduces the time and effort required to identify areas of interest, coverage, and the overall quality of the produced material. Unfortunately, optical microscopy has a low resolution, which is relatively poor compared to that of other methods and techniques [45].

Aberration-corrected HRTEM, on the other hand, offers atomic-resolution imaging, but requires the preparation of freely suspended samples [46] on rather delicate TEM grids. TEM sample preparation also contaminates 2D materials, and said contamination can only be removed with great effort [47, 48]. Eventually, even on relatively clean TEM samples, residual hydrocarbon contamination further reduces the already very small inspection areas of HRTEM. Another complication of the characterization of monolayer MoS_2 by HRTEM is the electron beam-induced damage that cannot be completely avoided, even at low acceleration voltages [49–53]. The creation of sulfur vacancies by the electron beam complicates the quantification of intrinsic defects and necessitates the recording and analysis of a large number of TEM images, as was the case in this work. Despite the straightforward structural information that is accessed by atomic-resolution imaging, this makes aberration-corrected HRTEM one of the most time-consuming techniques for characterizing CVD MoS_2.

By comparison, Raman and PL spectroscopies are much more time-efficient, and they reveal information about the crystal structure or electronic structure and can be used to probe the number of layers or structural stability but have low sensitivity. Additionally, the results can be distorted by significant background factors and heating through laser radiation can destroy the sample or mask the spectrum [54]. XPS is a spectroscopic technique that can identify elements and electronic structure but has the disadvantage of poor spatial resolution [55], and the results can be challenging to interpret [56]. C-V measurements are essential for monitoring and controlling the electrical characteristics of semiconductors; however, this technique is fundamentally limited to measurements in the depletion and weak inversion regimes only [57].

Based on optical microscopy, the following types of sample surface coverage were identified: small triangular MoS_2 flakes (samples A and B), connected large pockets of MoS_2 flakes (sample D), one large flake surrounded by a few smaller flakes (sample E), and continuous films MoS_2 (samples F and C). For better readability, **Figure 2** presents binarized optical images of MoS_2 of samples A, B, C, D, E, and F, respectively. Sample F achieved almost full yield coverage (99.98%) of the substrate. It is also worth noting that sample B had the highest coverage (53.13%) when only considering specimens with visible MoS_2 flakes (**Table 2**, Table S1).Regarding the intensities of Raman modes, sample B had the highest intensities of E^1_{2g} and A_{1g} with the most uniform distribution over the whole flake (Figures S3 and S4).The intensity ratio (E^1_{2g}/A_{1g}) was highest for sample A and lowest for sample C (**Table 2**). When comparing positions of Raman modes, sample A was the closest one to the overall average (E^1_{2g}: 385.73 [cm^{-1}] and A_{1g}: 406.22 [cm^{-1}]) in the case of E^1_{2g} and A_{1g}. Sample B had the lowest variation of E^1_{2g} and A_{1g} peak positions (**Table 2**, **Figure 2b**).

Analysis of Raman modes after MoS_2 was transferred onto new substrates for further device fabrication indicated that compressive and tensile stresses induced corresponding strains in the crystal, which were observed as shifts of a Raman peak position to higher or lower frequencies, respectively. The magnitude of the Raman peak shift was commensurate with that of the stress and corresponding strain induced in the material. The degree to which the Raman band will shift is dependent upon the specific material used, the elastic compliance constant of that chemical compound or element, and the distinct crystallographic axes being probed.

The highest photoluminescence intensity belonged to sample D. Sample F scored second place in this comparison (**Table 2**). After transfer, all PL spectra broadened (Figure S11) with visible patterns of higher- and lower-intensity streaks on the samples (Figure S12).

Based on the data presented in **Table 2** and **Figure 3**, as well as the information in Figure S16, our analysis using X-ray photoelectron spectroscopy revealed that sample E exhibited the lowest oxidation level before and after the transfer. Moreover, all the samples showed a decrease in oxidation level compared to their respective levels before the transfer, as indicated in Table S9.

Due to the vast array of parameters presented in this report, determining the most crucial features can be difficult. In **Figure 8**, we

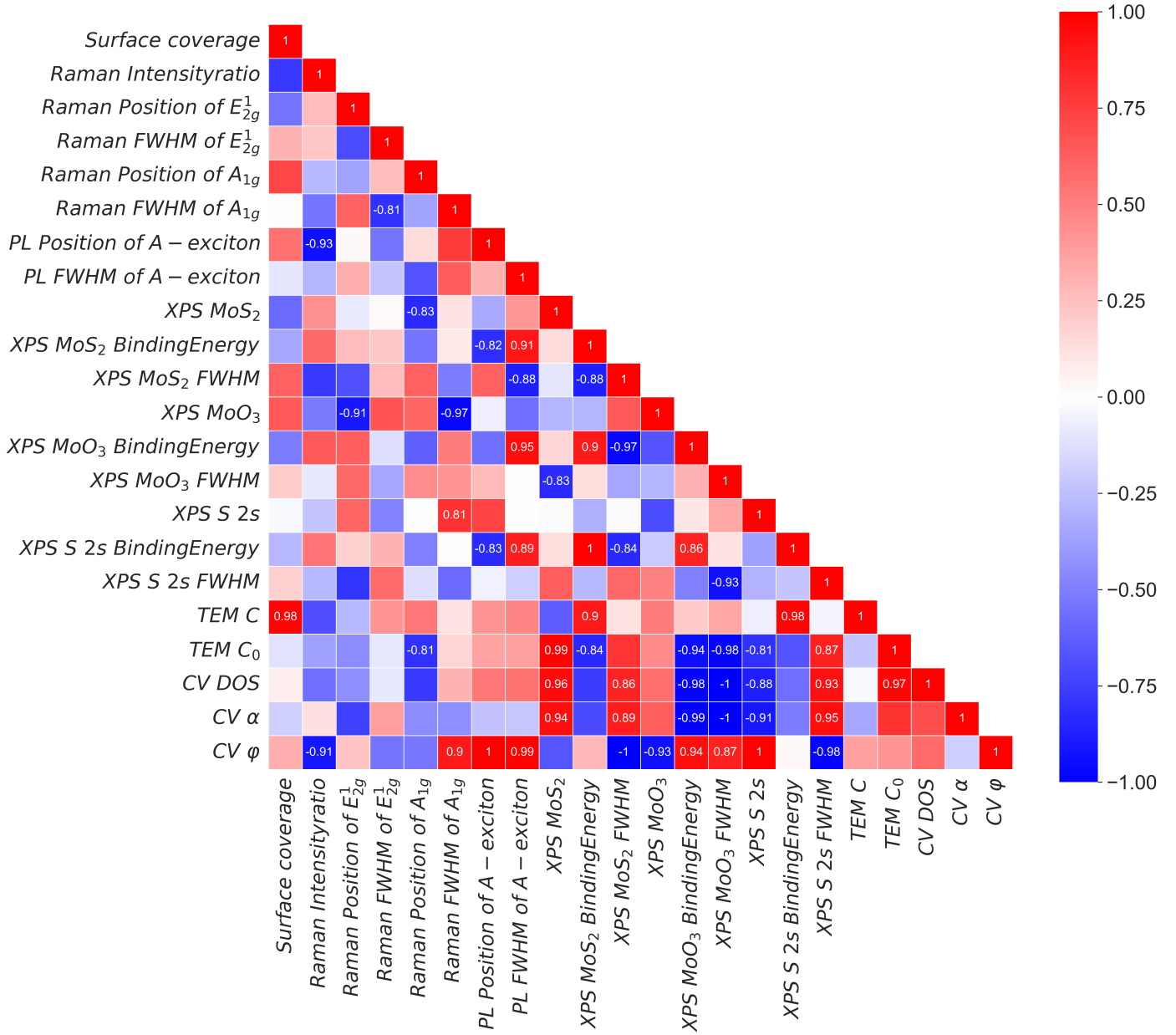


Figure 8 • Pearson correlation between extracted features.

have combined all the relevant parameters obtained from various measurements and assessed the correlation between the characteristics of the measured samples.

From the correlation color map, we could recognize the strong correlations among the following parameters: C-V ϕ value (highly correlated with nine other parameters), XPS MoO_3 binding energy (with seven parameters), CV DOS (with five parameters), CV α value (five), TEM defect density C_0 (four), XPS MoS_2 (four), XPS MoO_3 FWHM (four), and XPS S 2s FWHM (four). PL and Raman's measurement shows only a slight correlation with other parameters (1–2 high correlation values). These results confirm the high accuracy and correlation of TEM, C-V, and XPS measurement for defect characterization, which provides great insight for future quality assessment of MoS_2.

To demonstrate the ability of the data correlation plot and to highlight interesting relationships in **Figure 9**, we present a comparison of the features with the highest correlation values ($\rho > |0.92|$) and in Figure S17, we present a comparison of remaining features with correlation $\rho > |0.80|$.

We found a blue shift of the peak A from 1.78 eV to 1.88 eV, matching the increase in the Raman intensity ratio of E^1_{2g}/A_{1g} modes from 0.65 to almost 1.3 (**Figure 9a**, $\rho = 0.93$).

The full-width half maximums of Raman peaks are commonly used as indicators of the quality of the MoS_2 films, but we also established that, to be more precise, FWHM of A_{1g} mode can indicate oxidation of sample (**Figure 9b**, $\rho = 0.97$) and the FWHM of A-exciton can indicate binding energy of MoO_3 (**Figure 9e**, $\rho = 0.95$).

CV density of states—ϕ shows a strong correlation with the average position of A-exciton (**Figure 9d**, $\rho = 1$), Raman E^1_{2g}/A_{1g} intensity ratio (**Figure 9f**, $\rho = 0.91$), FWHM of A-exciton, and Raman FWHM of A_{1g} peak (Figure S17).

In **Figure 9c**, the trap density from CV is plotted against the density of intrinsic defects ($\rho = 0.97$), showing a clear correlation between the two quantities. Samples A and B, which showed the lowest and highest densities of sulfur vacancies in HRTEM, also

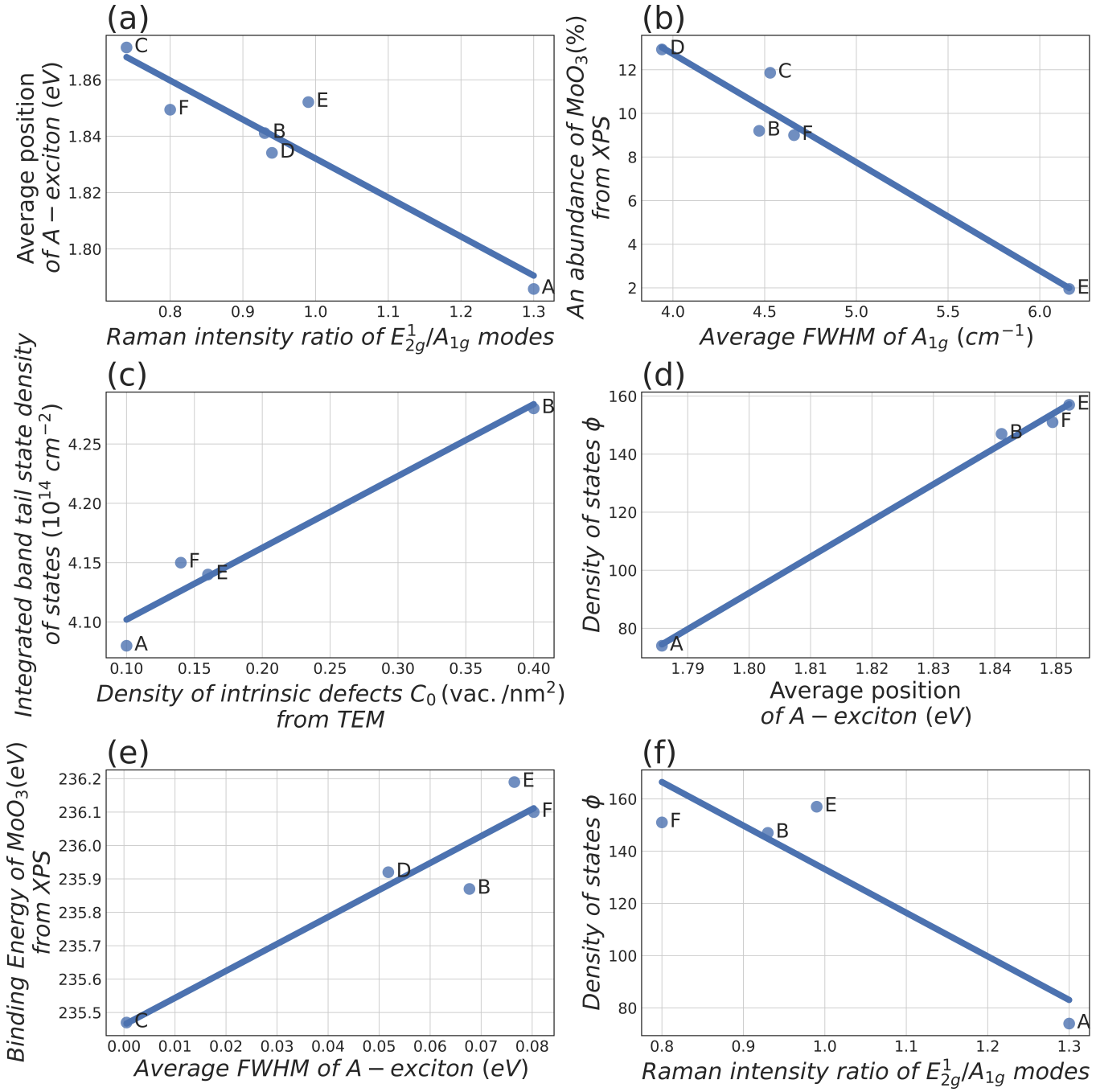


Figure 9 • An overview of the parameters with the highest correlation value from all measured properties. (**a**) Raman intensity ratio of E^1_{2g}/A_{1g} modes vs. average position of A-exciton. (**b**) Average FWHM of A_{1g} Raman peak vs. an abundance of MoO_3 (XPS). (**c**) Density of intrinsic defects C_0 vs. integrated band tail state density of states. (**d**) Average position of A-exciton vs. CV density of states—ϕ. (**e**) Average FWHM of A-exciton vs. binding energy of MoO_3 (XPS). (**f**) Raman intensity ratio of E^1_{2g}/A_{1g} modes vs. CV density of states ϕ.

have the lowest and highest trap densities, respectively. Accordingly, samples E and F, with their very similar defect densities, also have very similar trap density in the results of the CV measurements. Within the limits of accuracy of the defect densities from HRTEM, our results suggest that the trap densities increase linearly with the number of sulfur vacancies.

5. Summary

Each growth system has instrumental limitations that differ from those of other setups, such as workable pressures or temperature ranges. Furthermore, even if the primary parameters could be fully controlled, other factors like system and flow geometries, precise heating rates, or residual gas pressures can be more challenging, if not impossible, for researchers to replicate at different locations. All these factors influence the film's qualities. A comprehensive benchmarking study of the quality of CVD-grown TMD films, specifically MoS_2, has been undertaken. The most common and highly sophisticated methods characterized samples from six different sources. As a result, optical characterization can effectively determine the actual surface coverage. Raman and PL studies reveal the layer thickness and the quality of the material. However, HRTEM must be employed for more quantitative results, which can indicate defect densities. This data could be correlated with CV measurements, which show good agreement.

Acknowledgments

B.T. would like to thank Cormac Ó. Coileáin for constructive criticism of the manuscript.

Funding

The authors acknowledge the support of the European Union's Horizon 2020 research and innovation program under grant agreement No 785219 (Graphene Flagship). ERC Grants Hetero2D, GIPT, EU Grants GRAP-X, CHARM, EPSRC Grants EP/K01711X/1, EP/K017144/1, EP/N010345/1, EP/L016087/1, EP/V000055/1, EP/X015742/1.

Author contributions

A.K., U.K., M.G.H., C.B. and G.S.D. conceptualized the manuscript. B.T., B.M.S. and G.S.D. have developed the methodology. B.T., Y.Z., S.P., P.C. and C.P.C. synthesized the samples. B.T. performed optical, Raman, and photoluminescence measurements. O.H. performed X-ray photoelectron measurements and examined the acquired data. M.J.M., J.S. and T.L. performed TEM measurements and Y.Z. performed the MIS device fabrication and C-V measurements. B.T., M.J.M. and Y.Z. analyzed and interpreted the obtained data. N.M.E., C.C., A.C.F., P.K.S., S.M.S., A.R.C., I.P. and O.B. contributed to drafting and revising the manuscript. All authors have read and agreed to the published version of the manuscript.

Conflict of interest

The authors declare no conflicts of interest.

Data availability statement

Data supporting these findings are available within the article, at https://doi.org/10.20935/AcadNano7714, or upon request.

Institutional review board statement

Not applicable.

Informed consent statement

Not applicable.

Supplementary materials

The Supplementary materials are available at https://doi.org/10.20935/AcadNano7714. The following files contain additional figures and explanations, as described in the text, which are available free of charge as Supplementary materials containing detailed methods plots and descriptions. References [27, 40, 58] are cited in the Supplementary materials.

Additional information

Received: 2024-12-23

Accepted: 2025-05-08

Published: 2025-06-11

Academia Nano: Science, Materials, Technology papers should be cited as *Academia Nano: Science, Materials, Technology 2025*, ISSN 3065-9736, https://doi.org/10.20935/AcadNano7714. The journal's official abbreviation is *Acad. Nano: Sci. Mat. Tech.*

Publisher's note

Academia.edu Journals stays neutral with regard to jurisdictional claims in published maps and institutional affiliations. All claims expressed in this article are solely those of the authors and do not necessarily represent those of their affiliated organizations, or those of the publisher, the editors and the reviewers. Any product that may be evaluated in this article, or claim that may be made by its manufacturer, is not guaranteed or endorsed by the publisher.

Copyright

© 2025 copyright by the authors. This article is an open access article distributed under the terms and conditions of the Creative Commons Attribution (CC BY) license (https://creativecommons.org/licenses/by/4.0/).

References

1. Radisavljevic B, Radenovic A, Brivio J, Giacometti V, Kis A. Single-Layer MoS2 Transistors. Nat Nanotechnol. 2011;6(3):147–50. doi: 10.1038/nnano.2010.279
2. Jadwiszczak J, Maguire P, Cullen CP, Duesberg GS, Zhang H. Effect of localized helium ion irradiation on the performance of synthetic monolayer MoS 2 field-effect transistors. Beilstein J Nanotechnol. 2020;11:1329–35. doi: 10.3762/bjnano.11.117
3. Jariwala D, Sangwan VK, Late DJ, Johns JE, Dravid VP, Marks TJ, et al. Band-like transport in high mobility unencapsulated single-layer MoS2 transistors. Appl Phys Lett. 2013;102(17):173107. doi: 10.1063/1.4803920
4. George A, Fistul MV, Gruenewald M, Kaiser D, Lehnert T, Mupparapu R, et al. Giant persistent photoconductivity in monolayer MoS2 field-effect transistors. NPJ 2D Mater Appl. 2021;5(1):1–8 doi: 10.1038/s41699-020-00182-0
5. Bablich A, Schneider DS, Kienitz P, Kataria S, Wagner S, Yim C, et al. Few-Layer MoS2/a-Si:H Heterojunction Pin-Photodiodes for Extended Infrared Detection. ACS Photonics. 2019;6(6):1372–8. doi: 10.1021/acsphotonics.9b00337
6. De Fazio D, Goykhman I, Yoon D, Bruna M, Eiden A, Milana S, et al. High Responsivity, Large-Area Graphene/MoS2 Flexible Photodetectors. ACS Nano. 2016;10(9):8252–62.doi: 10.1021/acsnano.6b05109

7. Hinnemann B, Moses PG, Bonde J, Jørgensen KP, Nielsen JH, Horch S, et al. Biomimetic Hydrogen Evolution: MoS2 Nanoparticles as Catalyst for Hydrogen Evolution. J Am Chem Soc. 2005;127(15):5308–9. doi: 10.1021/ja0504690

8. Wu S, Huang H, Shang M, Du C, Wu Y, Song W. High visible light sensitive MoS2 ultrathin nanosheets for photoelectrochemical biosensing. Biosens Bioelectron. 2017;92:646–53. doi: 10.1016/j.bios.2016.10.037

9. Thakur M, Macha M, Chernev A, Graf M, Lihter M, Deen J, et al. Wafer-Scale Fabrication of Nanopore Devices for Single-Molecule DNA Biosensing using MoS2. Small Methods. 2020;4(11):2000072. doi: 10.1002/smtd.202000072

10. Lee K, Gatensby R, McEvoy N, Hallam T, Duesberg GS. High-Performance Sensors Based on Molybdenum Disulfide Thin Films. Adv Mater. 2013;25(46):6699–702. doi: 10.1002/adma.201303230

11. Yang X, Liu W, Xiong M, Zhang Y, Liang T, Yang J, et al. Au nanoparticles on ultrathin MoS2 sheets for plasmonic organic solar cells. J Mater Chem A. 2014;2:14798–806. doi: 10.1039/C4TA03178D

12. Barpuzary D, Banik A, Gogoi G, Qureshi M. Noble metal-free counter electrodes utilizing Cu2ZnSnS4 loaded with MoS2 for efficient solar cells based on ZnO nanowires co-sensitized with CuInS2-CdSe quantum dots. J Mater Chem A. 2015;3:14378–88. doi: 10.1039/C5TA03396A

13. Hu X, Chen L, Tan L, Zhang Y, Hu L, Xie B, et al. Versatile MoS2 Nanosheets in ITO-Free and Semi-transparent Polymer Power-generating Glass. Sci Rep. 2015;5(1):12161. doi: 10.1038/srep12161

14. Capasso A, Matteocci F, Najafi L, Prato M, Buha J, Cinà L, et al. Few-Layer MoS2 Flakes as Active Buffer Layer for Stable Perovskite Solar Cells. Adv Energy Mater. 2016;6(16):1600920. doi: 10.1002/aenm.201600920

15. Shastry TA, Balla I, Bergeron H, Amsterdam SH, Marks TJ, Hersam MC. Mutual Photoluminescence Quenching and Photovoltaic Effect in Large-Area Single-Layer MoS2-Polymer Heterojunctions. ACS Nano. 2016;10(11):10573–9. doi: 10.1021/acsnano.6b06592

16. Yoon Y, Ganapathi K, Salahuddin S. How Good Can Monolayer MoS2 Transistors Be? Nano Lett. 2011;11(9):3768–73. doi: 10.1021/nl2018178

17. Manzeli S, Dumcenco D, Migliato Marega G, Kis A. Self-sensing, tunable monolayer MoS2 nanoelectromechanical resonators. Nat Commun. 2019; doi: 10.1038/s41467-019-12795-1

18. Oviedo JP, KC S, Lu N, Wang J, Cho K, Wallace RM, et al. In Situ TEM Characterization of Shear-Stress-Induced Interlayer Sliding in the Cross Section View of Molybdenum Disulfide. ACS Nano. 2015;9(2):1543–51. doi: 10.1021/nn506052d

19. O'Brien M, McEvoy N, Hallam T, Kim HY, Berner NC, Hanlon D, et al. Transition Metal Dichalcogenide Growth via Close Proximity Precursor Supply. Sci Rep. 2014;4(1):7374. doi: 10.1038/srep07374

20. Sun J, Li X, Guo W, Zhao M, Fan X, Dong Y, et al. Synthesis methods of two-dimensional MoS2: A brief review. Crystals. 2017;7(7):198. doi: 10.3390/cryst7070198

21. Liu HF, Wong SL, Chi DZ. CVD Growth of MoS2-based Two-dimensional Materials. Chem Vapor Depos. 2015;21(10–12):241–59. doi: 10.1002/cvde.201500060

22. Samy O, Zeng S, Birowosuto MD, El Moutaouakil A. A Review on MoS2 Properties, Synthesis, Sensing Applications and Challenges. Crystals. 2021;11(4):355. doi: 10.3390/cryst11040355

23. Yu Y, Li C, Liu Y, Su L, Zhang Y, Cao L. Controlled Scalable Synthesis of Uniform, High-Quality Monolayer and Few-layer MoS2 Films. Sci Rep. 2013;3(1):1866. doi: 10.1038/srep01866

24. Van Rossum G, Drake FL Jr. Python reference manual. Amsterdam: Centrum voor Wiskunde & Informatica; 1995.

25. Virtanen P, Gommers R, Oliphant TE, Haberland M, Reddy T, Cournapeau D, et al. SciPy 1.0: Fundamental Algorithms for Scientific Computing in Python. Nat Methods. 2020;17:261–72. doi: 10.1038/s41592-019-0686-2

26. Hunter JD. Matplotlib: A 2D graphics environment. Comput Sci Eng. 2007;9(3):90–5. doi: 10.1109/MCSE.2007.55

27. Brivio J, Alexander DTL, Kis A. Ripples and Layers in Ultrathin MoS_2 Membranes. Nano Lett. 2011;11(12):5148–53. doi: 10.1021/nl2022288

28. Linck M, Hartel P, Uhlemann S, Kahl F, Müller H, Zach J, et al. Chromatic Aberration Correction for Atomic Resolution TEM Imaging from 20 to 80 kV. Phys Rev Lett. 2016;117(7):076101. doi: 10.1103/PhysRevLett.117.076101

29. Dumcenco D, Ovchinnikov D, Marinov K, Lazić P, Gibertini M, Marzari N, et al. Large-Area Epitaxial Monolayer MoS2. ACS Nano. 2015;9(4):4611–20. doi: 10.1021/acsnano.5b01281

30. Kim H, Ovchinnikov D, Deiana D, Unuchek D, Kis A. Suppressing Nucleation in Metal–Organic Chemical Vapor Deposition of MoS2 Monolayers by Alkali Metal Halides. Nano Lett. 2017;17(8):5056–63. doi: 10.1021/acs.nanolett.7b02311

31. Yanyuan Z, Xin L, Hai L, Jun Z, T AP, Kwan GC, et al. Interlayer Breathing and Shear Modes in Few-Trilayer MoS2 and WSe2. Nano Lett. 2013;2(13)1007–15. doi: 10.1021/nl304169w

32. Li H, Zhang Q, Yap CCR, Tay BK, Edwin THT, Olivier A, et al. From Bulk to Monolayer MoS2: Evolution of Raman Scattering. Adv Funct Mater. 2012;22(7):1385–90. doi: 10.1002/adfm.201102111

33. Nurunnabi M, McCarthy J. Biomedical Applications of Graphene and 2D Nanomaterials. Amsterdam: Elsevier; 2019.

34. Yin H, Zhang X, Lu J, Geng X, Wan Y, Wu M, et al. Substrate effects on the CVD growth of MoS2 and WS2. J Mater Sci. 2020;55:990–6. doi: 10.1007/s10853-019-03993-9

35. Wu Z, Ni Z. Spectroscopic investigation of defects in two-dimensional materials. Nanophotonics. 2017;6(6):1219–37. doi: 10.1515/nanoph-2016-0151

36. Lin Z, Carvalho BR, Kahn E, Lv R, Rao R, Terrones H, et al. Defect engineering of two-dimensional transition metal dichalcogenides. 2D Mater. 2016;3(2):022002. doi: 10.1088/2053-1583/3/2/022002

37. Wang D, Li XB, Han D, Tian WQ, Sun HB. Engineering two-dimensional electronics by semiconductor defects. Nano Today. 2017;16:30–45. doi: 10.1016/j.nantod.2017.07.001

38. George A, Neumann C, Kaiser D, Mupparapu R, Lehnert T, Hübner U, et al. Controlled growth of transition metal dichalcogenide monolayers using Knudsen-type effusion cells for the precursors. J Phys Mater. 2019;2(1):016001. doi: 10.1088%2F2515-7639%2Faaf982

39. Kim IS, Sangwan VK, Jariwala D, Wood JD, Park S, Chen KS, et al. Influence of Stoichiometry on the Optical and Electrical Properties of Chemical Vapor Deposition Derived MoS2. ACS Nano. 2014;8(10):10551–8. doi: 10.1021/nn503988x

40. Shree S, George A, Lehnert T, Neumann C, Benelajla M, Robert C, et al. High optical quality of MoS2 monolayers grown by chemical vapor deposition. 2D Mater. 2019;7(1):015011. doi: 10.1088%2F2053-1583%2Fab4f1f

41. Lehtinen O, Komsa HP, Pulkin A, Whitwick MB, Chen MW, Lehnert T, et al. Atomic Scale Microstructure and Properties of Se-Deficient Two-Dimensional $MoSe_2$. ACS Nano. 2015;9(3):3274–83. doi: 10.1021/acsnano.5b00410

42. Zhu W, Low T, Lee YH, Wang H, Farmer DB, Kong J, et al. Electronic Transport and Device Prospects of Monolayer Molybdenum Disulphide Grown by Chemical Vapour Deposition. Nat Commun. 2014;5(1):3087. doi: 10.1038/ncomms4087

43. Zhou W, Zou X, Najmaei S, Liu Z, Shi Y, Kong J, et al. Intrinsic Structural Defects in Monolayer Molybdenum Disulfide. Nano Lett. 2013;13(6):2615–22. doi: 10.1021/nl4007479

44. Bertolazzi S. Charge-Transport Properties of Monolayer MoS2 at the Interface with Dielectric Materials. Lausanne: EPFL; 2015.

45. Aleithan SH, Mahmoud-Ghoneim D. Toward automated classification of monolayer versus few-layer nanomaterials using texture analysis and neural networks. Sci Rep. 2020;10(1):20663. doi: 10.1038/s41598-020-77705-8

46. Meyer JC, Geim AK, Katsnelson MI, Novoselov KS, Booth TJ, Roth S. The structure of suspended graphene sheets. Nature. 2007;446(7131):60–3. doi: 10.1038/nature05545

47. Longchamp JN, Escher C, Fink HW. Ultraclean freestanding graphene by platinum-metal catalysis. J Vac Sci Technol B. 2013;31(2):020605. doi: 10.1116/1.4793746

48. Algara-Siller G, Lehtinen O, Turchanin A, Kaiser U. Dry-cleaning of graphene. Appl Phys Lett. 2014;104(15):153115. doi: 10.1063/1.4871997

49. Komsa HP, Kotakoski J, Kurasch S, Lehtinen O, Kaiser U, Krasheninnikov AV. Two-Dimensional Transition Metal Dichalcogenides under Electron Irradiation: Defect Production and Doping. Phys Rev Lett. 2012;109(3):035503. doi: 10.1103/PhysRevLett.109.035503

50. Zan R, Ramasse QM, Jalil R, Georgiou T, Bangert U, Novoselov KS. Control of Radiation Damage in MoS2 by Graphene Encapsulation. ACS Nano. 2013;7:10167–74. doi: 10.1021/nn4044035

51. Algara-Siller G, Kurasch S, Sedighi M, Lehtinen O, Kaiser U. The pristine atomic structure of MoS2 monolayer protected from electron radiation damage by graphene. Appl Phys Lett. 2013;103:203107. doi: 10.1063/1.4830036

52. Kretschmer S, Lehnert T, Kaiser U, Krasheninnikov AV. Formation of Defects in Two-Dimensional MoS2 in the Transmission Electron Microscope at Electron Energies below the Knock-on Threshold: The Role of Electronic Excitations. Nano Lett. 2020;20:2865–70. doi: 10.1021/acs.nanolett.0c00670

53. Susi T, Meyer JC, Kotakoski J. Quantifying transmission electron microscopy irradiation effects using two-dimensional materials. Nat Rev Phys. 2019;1:397–405. doi: 10.1038/s42254-019-0058-y

54. Skoog DA, Holler FJ, Crouch SR. Principles of Instrumental Analysis. International student edition. Thomson Brooks/Cole; Boston (MA): Cengage Learning; 2007 [cited 2024 Nov 1]. Available from: https://books.google.de/books?id=GrOsQgAACAAJ.

55. Lasek K, Li J, Kolekar S, Coelho PM, Guo L, Zhang M, et al. Synthesis and characterization of 2D transition metal dichalcogenides: Recent progress from a vacuum surface science perspective. Surf Sci Rep. 2021;76(2):100523. doi: 10.1016/j.surfrep.2021.100523

56. Greczynski G, Hultman L. The same chemical state of carbon gives rise to two peaks in X-ray photoelectron spectroscopy. Sci Rep. 2021;11:11195. doi: 10.1038/s41598-021-90780-9

57. Hack J, Luderer C, Reichel C, Opila R, Bivour M. Determining limitations of capacitance-voltage measurements of built-in voltage as an alternative to surface photovoltage for a-Si:H/c-Si heterojunctions. Solar Energy Mater Solar Cells. 2021;219:110794. doi: 10.1016/j.solmat.2020.110794

58. Luo S, Cullen CP, Guo G, Zhong J, Duesberg GS. Investigation of growth-induced strain in monolayer MoS2 grown by chemical vapor deposition. Appl Surface Sci. 2020; doi: 10.1016/j.apsusc.2019.145126